Mountains on Titan: Modeling and observations

Giuseppe Mitri,[1] Michael T. Bland,[2] Adam P. Showman,[3] Jani Radebaugh,[4] Bryan Stiles,[5] Rosaly M. C. Lopes,[5] Jonathan I. Lunine,[6,7] and Robert T. Pappalardo[5]

Received 24 February 2010; revised 12 May 2010; accepted 25 June 2010; published 12 October 2010.

[1] We have developed a thermal model of Titan's interior to study changes in volume during partial freezing or melting of a subsurface ocean due to heat flux variations from the interior. We find that the long-term cooling of Titan can cause global volume contraction $\Delta V/V \sim 0.01$. We then simulate two-dimensional contractional deformation of Titan's icy lithosphere, finding that contractional deformation can produce tectonic activity and fold formation. Folds could potentially achieve a topographic height of several kilometers for high local strain (~0.16), and for high temperature gradients in the ice I shell (order of 10 K km^{-1}), corresponding to an ancient high heat flux from the interior (order of 0.02–0.06 W m^{-2}). Examination of Synthetic Aperture Radar (SAR) imagery obtained by Cassini Radar shows possible evidence of contractional tectonism in the equatorial regions of Titan, although the moderate resolution of the Cassini SAR imagery does not permit an unambiguous geological interpretation.

Citation: Mitri, G., M. T. Bland, A. P. Showman, J. Radebaugh, B. Stiles, R. M. C. Lopes, J. I. Lunine, and R. T. Pappalardo (2010), Mountains on Titan: Modeling and observations, *J. Geophys. Res.*, *115*, E10002, doi:10.1029/2010JE003592.

1. Introduction

[2] The Cassini Radar instrument has imaged mountainous topography on Saturn's moon Titan [*Radebaugh et al.*, 2007]. Tectonic activity on icy satellites of the outer solar system may be related to different global processes such as tides, despinning, nonsynchronous rotation, polar wander, and volume changes. Other processes can produce tectonic features on icy satellites such as thermal convection in the ice I shell and diapirism. *Collins et al.* [2009] present a comprehensive review on tectonic processes of icy satellites.

[3] The interior of Titan is inferred to be at least partially differentiated into a rocky interior or a deep interior composed of a mixture of ice and rock, a high-pressure (HP) ice layer (with phases III, V, and VI), a subsurface ocean, and an outer ice I shell [*Grasset et al.*, 2000; *Sohl et al.*, 2003; *Tobie et al.*, 2005, 2006; *Mitri and Showman*, 2008; *Mitri et al.*, 2010]. Titan's normalized axial moment of inertia as inferred by gravity coefficients and hydrostatic equilibrium theory with Radau-Darwin approximation is $C/MR^2 \sim 0.34$ [*Iess et al.*, 2010]. *Mitri et al.* [2010] have shown that Titan's deep interior (≤2,100 km radius) is likely composed of a mixture of ice and rock indicating a partial differentiation. Accretion models [*Mousis et al.*, 2002] and mass spectrometric measurements [*Niemann et al.*, 2005; *Waite et al.*, 2005] suggest that ammonia might be present within Titan. In Titan's early history, ammonia and other volatiles were likely released during the accretion and differentiation stages [*Lunine and Stevenson*, 1987]. At the present time, an ammonia-water subsurface ocean could be present based on thermal evolution considerations [*Tobie et al.*, 2005, 2006; *Mitri and Showman*, 2008]. Interpretation of Titan' spin rate [*Lorenz et al.*, 2008; *Stiles et al.*, 2008] and long wavelength topography [*Nimmo and Bills*, 2010] provide indirect evidence of the existence of a subsurface liquid layer on Titan. The hypothesis that ammonia is present within Titan is strengthened by the recent detection of ammonia on Enceladus [*Waite et al.*, 2009]. Within Titan's subsurface liquid layer salts also might be present (see section 5). Large amounts of sulfur have been invoked to explain resurfacing processes on Titan [*Fortes et al.*, 2007]. However, radiometric data from the Cassini spacecraft is not consistent with the presence of large amount of sulfates on Titan's surface [*Paganelli et al.*, 2007]. Therefore, here we will consider that ammonia is the main component of a subsurface water ocean.

[4] During its thermal-orbital evolution, Titan is expected to have experienced a gradual cooling [*Tobie et al.*, 2005, 2006]. Here we develop a thermal model of Titan's interior to model the predicted change in volume due to the long-term cooling of Titan, predicting contraction. We then simulate two-dimensional contractional deformation of Titan's icy lithosphere to investigate whether global volume changes can produce tectonic activity and fold formation on Titan,

[1]Division of Geological and Planetary Sciences, California Institute of Technology, Pasadena, California, USA.
[2]Department of Earth and Planetary Sciences, Washington University, Saint Louis, Missouri, USA.
[3]Department of Planetary Sciences and Lunar and Planetary Laboratory, University of Arizona, Tucson, Arizona, USA.
[4]Department of Geological Sciences, Brigham Young University, Provo, Utah, USA.
[5]Jet Propulsion Laboratory, California Institute of Technology, Pasadena, California, USA.
[6]Department of Physics, University of Rome Tor Vergata, Rome, Italy.
[7]Institute for the Physics of Interplanetary Space, INAF, Rome, Italy.

0148-0227/10/2010JE003592

Table 1. Physical Parameters

Parameter	Variable	Value
Mass of Titan	M_T	$1.345 \cdot 10^{23}$ kg
Radius of Titan	R_T	2,575 km
Gravity	g	1.35 m s^{-2}
Surface temperature	T_s	94 K
Thermal expansivity of ice	α'	$1.6 \cdot 10^{-4}$ K
Thermal diffusivity of ice	κ	$1.3 \cdot 10^{-6}$ m^2 s^{-1}
Heat capacity of seawater	c_p	3,900 J kg^{-1} K^{-1}
Young's modulus of ice	E	$9 \cdot 10^9$ Pa
Poisson's ratio of ice	ν	0.314

predicting the occurrence of folds. Finally, we use Cassini Radar Synthetic Aperture Radar (SAR) imagery, altimetry data, and topography obtained by SARTopo and radarclinometric techniques to consider possible observational evidence for contractional tectonic features on Titan.

2. Global Volume Changes

2.1. Model

[5] Here we model the change in Titan's volume during its evolution by expanding upon the thermal model of *Mitri and Showman* [2008].

2.1.1. Thermal Model of Ice I Shell

[6] *Mitri and Showman* [2008] presented a thermal model of Titan's ice I shell in order to understand ice I shell dynamics, considering that thermal convection can occur in the ice I shell in the stagnant lid regime under a range of conditions. With this model, the authors determined the thickness and thermal state (conductive versus convective) of the ice I shell using a convective scaling law. Here a more complex model is created in order to consider resulting global volume changes throughout Titan's evolution. Here we briefly describe the model of *Mitri and Showman* [2008].

[7] Because of the low tidal and convective stresses in Titan's ice shell, the predominant creep mechanisms are expected to be superplastic deformation with grain boundary sliding (GBS) in combination with diffusion [*Mitri and Showman*, 2008]. Volume diffusion dominates over GBS in Titan's convecting ice shell for grain size smaller than ~1 mm [*Mitri and Showman*, 2008]. Therefore, we consider that diffusion creep is the dominant creep mechanism of water ice within the ice I shell [*Durham et al.*, 1997; *McKinnon*, 1999, 2006; *Mitri and Showman*, 2005, 2008].

[8] The ice viscosity can be written as

$$\eta = \frac{RTd^2}{3A'\Omega D_0} e^{\frac{Q}{RT}} \tag{1}$$

where we adopt the constant $A' = 14$, the molar volume $\Omega = 1.97 \cdot 10^{-5}$ m^3, the coefficient $D_0 = 9.1 \cdot 10^{-4}$ m^2 s^{-1}, and the activation energy $Q = 59.4$ kJ mol^{-1} [*McKinnon*, 2006]. T is the temperature and R is the gas constant. We consider that the ice grain size d ranges between 0.1 mm and 1 mm [*McKinnon*, 2006; *Mitri and Showman*, 2008].

[9] The model adopts the *Dumoulin et al.* [1999] scaling law of thermal convection in the stagnant lid regime. The Rayleigh number defined at the base of the ice shell is given by

$$Ra_b = \frac{\alpha' \rho_{ice} g \Delta T \delta^3}{\kappa \eta_b} \tag{2}$$

where α' ($1.6 \cdot 10^{-4}$ K^{-1}) is the thermal expansivity of the ice, ρ_{ice} (920 kg m^{-3}) is ice density, g (1.35 m s^{-2}) is Titan's surface gravity, ΔT is the temperature difference between the bottom and the surface of the ice I shell, δ is the thickness of the ice shell, κ ($1.3 \cdot 10^{-6}$ m^2 s^{-1}) is the thermal diffusivity, and η_b is the viscosity at the bottom of the ice I shell. The physical parameters used in the model are summarized in Table 1. The Rayleigh number defined in the convective layer's interior is given by

$$Ra_i = \frac{\alpha' \rho_{ice} g \Delta T \delta^3}{\kappa \eta_i} \tag{3}$$

where η_i is the viscosity within the interior of the convective sublayer. The ratio between these Rayleigh numbers is [*Solomatov and Moresi*, 1996; *McKinnon*, 2006]

$$Ra_b \sim e \cdot Ra_i \tag{4}$$

where e is the Euler's number. The dependence of the Nusselt number Nu on the Rayleigh number Ra_i is, for low Rayleigh number [*Dumoulin et al.*, 1999]

$$Nu = 1.99\theta^{-1} Ra_i^{1/5} \tag{5}$$

and for higher Rayleigh number

$$Nu = 0.52\theta^{-4/3} Ra_i^{1/3} \tag{6}$$

The parameter θ is given by

$$\theta = 1.2 \frac{Q \Delta T}{R T_i^2} \tag{7}$$

where T_i is the temperature in the interior of the convective sublayer. The temperature difference between the base of the ice I shell and the convective interior is [*Solomatov and Moresi*, 2000]

$$T_b - T_i \sim \frac{RT_i^2}{Q} \tag{8}$$

where T_b is the temperature at the base of the shell.

[10] The critical Rayleigh number defined at the bottom of the ice I shell assuming Newtonian rheology (diffusion creep) is given by [*Solomatov*, 1995]

$$Ra_{b,cr} = 20.9\theta^4 \tag{9}$$

To take into account the spherical geometry of Titan and the temperature dependence of the thermal conductivity, we approximate the surface heat flux as in the work of *McKinnon* [2006] and *Mitri and Showman* [2008]

$$F = \frac{621}{\delta'} \ln\left(\frac{T_b}{T_s}\right)\left(1 - \frac{\delta'}{R_T}\right) Nu \text{ W m}^{-1} \tag{10}$$

where T_s is the surface temperature (94 K), δ' is the effective thickness of the ice I shell and R_T is the satellite radius.

2.1.2. Global Volume Change Model

[11] *Mitri and Showman* [2008] suggested that the thermal evolution of Titan would have important implications for the surface tectonics. This hypothesis is explored here by

Table 2. Reference Density ρ_0, Pressure Derivative of the Bulk Modulus K_0', and the Bulk Modulus K_0

	ρ_0 (kg m^{-3})	K_0 (GPa)	K_0'	Reference
Ammonia-water liquid	1,000	2.5	5.0	*Croft et al.* [1988]
Ice I	920	9.2	5.5	*Sotin et al.* [1998]
Ice III	1,140	8.5	5.7	*Sotin et al.* [1998]
Ice V	1,235	13.2	5.2	*Sotin et al.* [1998]
Ice VI	1,320	14.9	6.6	*Sotin et al.* [1998]

examining the satellite's volumetric changes over the course of its evolution. In order to model global volume changes, in addition to the ice I shell the model includes a subsurface liquid layer, as well as a high-pressure ice layer (with ice phases III, V and VI). Furthermore, different possible scenarios for both fully and partially differentiated interior structures are investigated. We consider that the interior of Titan is differentiated into a central interior composed of rock or a mixture of ice and rock, a high-pressure ice layer with phase III (reference density 1,140 kg m^{-3}), phase V (reference density 1,235 kg m^{-3}) and phase VI (reference density 1,320 kg m^{-3}), a subsurface ocean (reference density 1,000 kg m^{-3}), and an outer ice I shell (reference density 920 kg m^{-3}).

[12] We assume a maximum initial ammonia mass concentration in the liquid layer ranging between 0 and 5%, consistent with ammonia concentrations observed in comets and Enceladus [*Waite et al.*, 2009]. We assume that the subsurface ocean is in thermal equilibrium with the ice I shell and at the melting temperature of the ice. We use the phase diagram of water as in the work of *Grasset et al.* [2000] and *Choukroun and Grasset* [2007].

[13] The temperature of the interface between the ice I shell and the ocean can be found from the ammonia-water phase diagram [*Grasset et al.*, 2000; *Choukroun and Grasset*, 2007]. The basal temperature of the ocean is determined assuming it is adiabatic and equating the temperature at the base of the ocean to the phase diagram of water ice. The temperature and pressure at the base of the ocean determine the phases of the ice high-pressure layer. The adiabatic temperature of the ocean is determined solving the equation

$$\frac{dT}{dP} = \frac{\alpha'' T}{\rho_w c_p} \tag{11}$$

where α'' is the pressure-dependent thermal expansion coefficient [*Bland et al.*, 2009], ρ_w is the water density and c_p is the heat capacity of the seawater (3,900 J kg^{-1} K^{-1}) [*Mamayev*, 1975], T is the temperature, and P is the pressure.

[14] The pressure dependence of the density of ice I, III, V, VI and liquid water is written as

$$\rho(P) = \rho_0 \left[\frac{K_0'}{K_0} P + 1 \right]^{\frac{1}{K_0'}} \tag{12}$$

where ρ_0 is the reference density, and K_0' and K_0 are the pressure derivatives of the bulk modulus and the bulk modulus, respectively. The values of ρ_0, K_0' and K_0 are given in Table 2.

[15] We assume that Titan's present heat flux given by radiogenic and tidal contributions is 0.007 W m^{-2} [*Tobie et al.*, 2005; *Mitri and Showman*, 2008], the present radius is 2,575 km, and the mass is constant during its thermal evolution ($M_T = 1.345 \cdot 10^{23}$ kg). The triple point pressure of ice III is at 209.5 MPa, ice V is at 355.0 MPa, and ice VI is at 618.4 MPa [*Choukroun and Grasset*, 2007]. These parameter values allow computation of the volume, mass, and thickness of each layer (ice I, III, V and VI shells, and the ocean) as a function of the heat flow from the interior.

2.2. Results

[16] This section examines the model results in terms of global volume change. Here we also examine the effects on global volume change of the onset of convection in the ice I shell, the internal differentiation, and the ammonia-water concentration.

[17] Figure 1 summarizes the results of the global volume change model of Titan's interior. The model shows the variations in the dimensions of the whole satellite radius, the ice I shell, the ocean, and the high-pressure ice layer (with phases III, V and VI) as a function of the heat flux, for an initial 5% ammonia-water concentration in the ocean. For this model, the density of the rocky interior is 3,300 kg m^{-3} and the rocky core radius is 1,780 km. We present the model's results for two ice I grain sizes (Figures 1a and 1b for 0.1 mm, and Figures 1c and 1d for 1.0 mm). The white and gray areas show where the heat flux is transported by thermal conduction and thermal convection in the ice I shell, respectively. The darker gray areas indicate where the thermal convection in the ice I shell is in a subcritical state. Thermal conduction and thermal convection in subcritical state for the ice I shell of Titan is discussed in detail by *Mitri and Showman* [2008]. Figure 1 shows that for an initial ammonia water concentration of 5% and ice grain size of 0.1 mm, thermal convection occurs over a heat flux range of $0.007 < F < 0.032$ W m^{-2}, suggesting that after a transient period of thermal convection, the ice I shell could be in a conductive state at the present time [see also *Mitri and Showman*, 2008].

[18] The cooling of Titan (corresponding to the heat flux decreasing in Figure 1) produces thickening of the ice I, III, V and VI layers, and the freezing of the subsurface ocean. Because of the density differences among the ice I layer, high-pressure ice layer, and the liquid layer, the long-term cooling of Titan and simultaneous freezing of the ice I and high-pressure ice layers causes a global radial contraction (Figure 1). For example, for an ice I grain size of 0.1 mm and an initial ammonia water concentration of 5%, considering values at the onset of convection ($F \sim 0.032$ W m^{-2}) and a temperature gradient of ~9 K km^{-1}, the resultant radial contraction is ~7 km and the global volume contraction is $\Delta V/V \sim 0.008$ from the onset of convection to the present heat flux of 0.007 W m^{-2} (Figures 1a and 1b).

[19] How do the thermal state of the ice I shell and the onset of convection affect the global volume change? Interior heat production (radiogenic and tidal) varies during the evolution of Titan, and the consequent volume contraction occurs over a time scale of the order of 10^8–10^9 yr [*Tobie et al.*, 2005, 2006]. However, because of the dependence of melting temperature on pressure, the onset of convection in the ice shell produces a rapid thickening of the ice shell

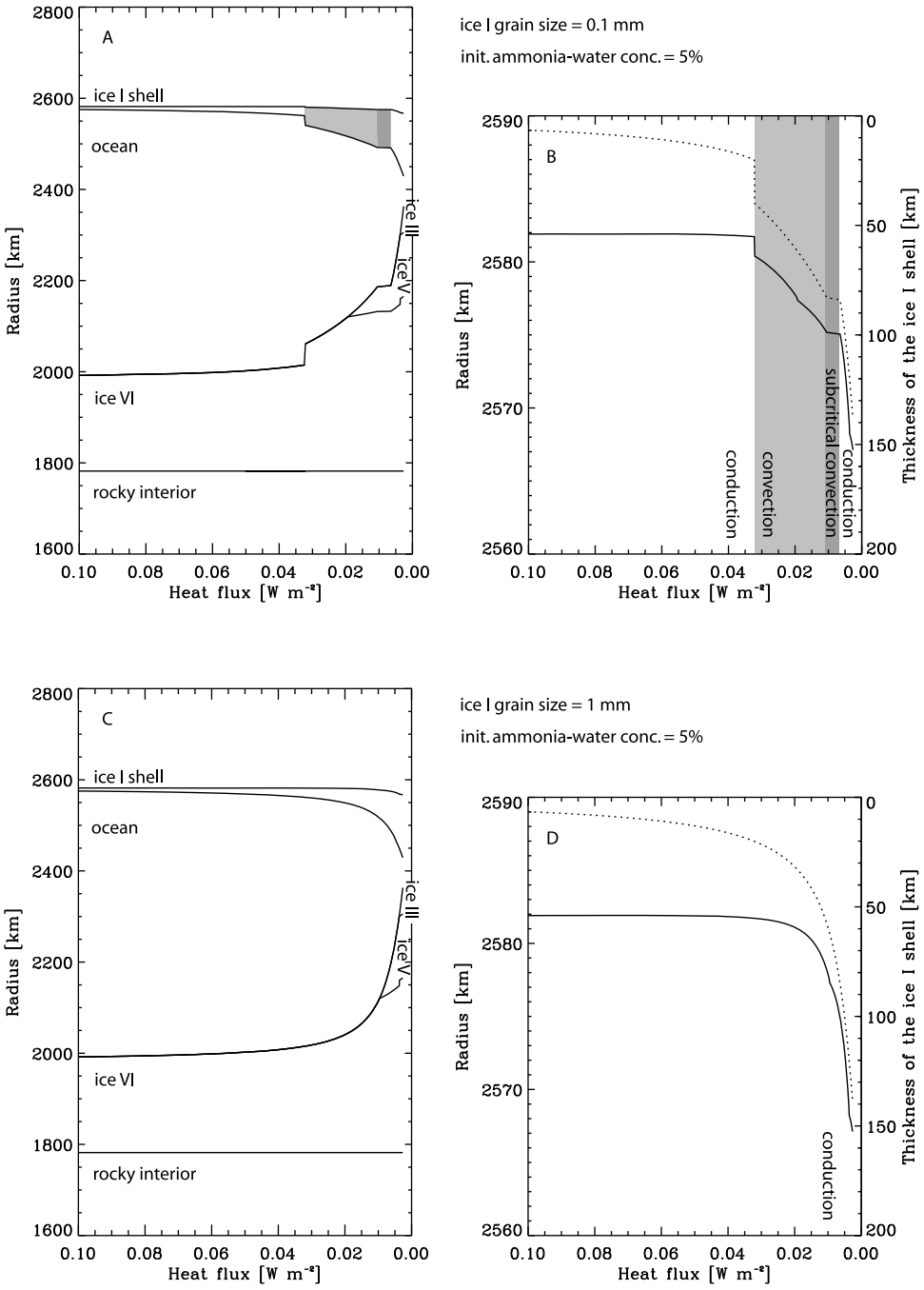

Figure 1. Radius versus heat flux during the long-term cooling of Titan, which produces radial contraction and consequent contractional lithospheric deformation in the ice I shell. (a) The thermal evolution of the radius, ice I shell, ocean, and high-pressure ice layer (with phases III, V and VI) for an initial ammonia-water concentration in the ocean of 5% and an ice I grain size of 0.1 mm. The reference density of the liquid water is 1,000 kg m^{-3}. The white and gray areas show where the heat flux is transported by thermal conduction and thermal convection in the ice I shell, respectively. The darker gray areas show where thermal convection in the ice I shell is in a subcritical state (for discussion of convection in subcritical state see *Mitri and Showman* [2008]). (b) The evolution of the radius (solid line) and thickness of the ice I shell (dotted line), as in Figure 1a. (c and d) The model for an ice I grain size of 1 mm and an initial ammonia-water concentration of 5%.

and simultaneous thickening of the ice high-pressure layer, causing a large and rapid radial contraction of ~2 km (Figures 1a and 1b) over a time scale of ~10^7 yr. Also, the radius of Titan depends on the thermal state of the ice I shell. For example, for a heat flux equal to 0.04 W m^{-2}, the ice I shell is in a conductive state for both grain sizes d = 0.1 mm and d = 1.0 mm, and the satellite radius is ~2,582 km (Figure 1). For a heat flux equal to 0.03 W m^{-2}, for d = 0.1 mm the ice shell is in convective state and the radius is ~2,580 km (Figures 1a and 1b); whereas for d = 1 mm, the ice shell is in conductive state and the radius is ~2,582 km (Figures 1c and 1d).

[20] Another question is how Titan's internal differentiation affects the global volume change during the cooling of the interior. The presence or absence of a high-pressure ice layer in the interior principally determines whether an icy satellite will contract or expand during cooling. For example, the interior of Europa is likely differentiated into a rocky interior, a subsurface ocean, and an outer ice I shell [e.g., *Anderson et al.*, 1998; *Mitri and Showman*, 2005]. Unlike Titan, Europa lacks a high-pressure ice layer; consequently, thickening of Europa's ice I shell causes radial expansion, which might produce extensional tectonic features such as fractures or bands [*Nimmo*, 2004; *Mitri and Showman*, 2005; *Manga and Wang*, 2007]. The core radius does not affect the functional dependence of the depth from the surface of the high-pressure ice layer. Therefore, if the model in Figure 1 is altered to a partially differentiated Titan, decreasing the core density in the model predicts a larger core radius and a thinner high-pressure ice layer than the model of Figure 1. However, the thickness of the ice I shell and liquid layer, the depth of the high-pressure ice layer as measured from the surface of Titan, and the associated volume changes are equal to the model of Figure 1.

[21] In the model of Figure 1, we have considered that ammonia is the main component of the subsurface liquid water layer, and we have adopted a reference density of the liquid layer of 1,000 kg m^{-3} for equation (12). The presence of ammonia in a liquid sublayer is supported by accretion and differentiation models of Titan [*Lunine and Stevenson*, 1987] as well as the observations in comets and Enceladus [*Waite et al.*, 2009] as mentioned in the introduction of this paper. But what is the contribution of ammonia to the global volume change in terms of density of the subsurface ocean? Ammonia decreases the mean density of the liquid layer and makes it easier for global radial contraction to occur as Titan cools. In fact, the peritectic ammonia-water liquid with a composition near that of pure ammonia dihydrate has a density of 946 kg m^{-3}, which is lower than the liquid water density (1,000 kg m^{-3}). Therefore, ammonia within the liquid layer reduces the difference between the density of the ice I shell and the liquid layer, reducing the effect of the expansion of the ice I layer during Titan's cooling. At the same time, the ammonia increases the difference between the density of the high-pressure ice layer and the liquid layer, increasing the effect of the expansion of the high-pressure ice layer during the freezing of the ocean. Overall increasing the ammonia concentration increases the global volume contraction. Because the reference density for the model is 1,000 kg m^{-3}, we have verified that for a small ammonia-water concentration and at the limit of a pure water ocean, global radial contraction occurs during Titan's cooling.

[22] In summary, we have shown that the cooling of Titan over its evolution leads to a global radial contraction under a range of conditions. In section 3, we will discuss and model the implications of radial contraction on Titan's surface geology.

3. Modeling Lithospheric Shortening

[23] Radial contraction of Titan during its cooling can produce lithospheric shortening. This leads us to consider the predicted tectonic implications of such radial contraction.

3.1. Tekton Model

[24] We simulate two-dimensional contractional deformation of Titan's lithosphere in a state of plane strain using the Tekton model [*Melosh and Raefsky*, 1980], as modified by *Bland and Showman* [2007]. Tekton is a finite element code developed to solve tectonic problems. The model is elastic-viscous-plastic and uses the composite rheology of the water ice (see below). A Cartesian domain is a good approximation of Titan's near-surface deformation, because the thickness of the lithosphere is much less than the Titan's radius.

[25] Non-Newtonian viscoelastic constitutive equations are written as [*Melosh and Raefsky*, 1980]

$$\dot{\varepsilon}_{xx} = \frac{(1+\nu)}{E}\left[(1-\nu)\dot{\sigma}_{xx} - \nu\dot{\sigma}_{yy}\right] + \frac{\sigma^{n-1}}{4\eta}\left[\sigma_{xx} - \sigma_{yy}\right] \quad (13)$$

$$\dot{\varepsilon}_{yy} = \frac{(1+\nu)}{E}\left[(1-\nu)\dot{\sigma}_{yy} - \nu\dot{\sigma}_{xx}\right] - \frac{\sigma^{n-1}}{4\eta}\left[\sigma_{xx} - \sigma_{yy}\right] \quad (14)$$

$$\dot{\varepsilon}_{xy} = \frac{(1+\nu)}{E}\dot{\sigma}_{xy} + \frac{\sigma^{n-1}}{2\eta}\sigma_{xy} \quad (15)$$

where

$$\sigma = \sqrt{\left(\frac{\sigma_{xx} - \sigma_{yy}}{2}\right)^2 + \sigma_{xy}^2} \quad (16)$$

and η is the viscosity, E is the Young's modulus, ν is Poisson's ratio, σ_{ij} is the stress tensor, and ε_{ij} is the strain tensor with i, j tensorial indices.

[26] The elastic behavior of ice is characterized by the Young's modulus E and Poisson's ratio ν. *Gammon et al.* [1983] have determined that Young's modulus for terrestrial sea ice is ~$9{\cdot}10^9$ Pa. Poisson's ratio is assumed to be fixed at 0.314 [*Hutter*, 1983], and the ice I density is taken as 920 kg m^{-3}.

[27] The constitutive rheologies of the viscous flow are based on laboratory measurements [*Kirby et al.*, 1987; *Durham et al.*, 1997; *Goldsby and Kohlstedt*, 2001]. The several deformation mechanisms of ice I are accounted for by a composite equation [*Goldsby and Kohlstedt*, 2001; *Bland and Showman*, 2007] written as

$$\dot{\varepsilon} = \dot{\varepsilon}_{diff} + \left(\frac{1}{\dot{\varepsilon}_{basal}} + \frac{1}{\dot{\varepsilon}_{gbs}}\right)^{-1} + \dot{\varepsilon}_{dca} + \dot{\varepsilon}_{dcb} + \dot{\varepsilon}_{dcc} \quad (17)$$

Table 3. Rheological Parameters

Deformation Creep[a]	Log A (MPa^{-n} m^m s^{-1})	m	n	Q (kJ mol^{-1})	Reference
dca	11.8	0	4.0	91	*Kirby et al.* [1987]
dcb	5.1	0	4.0	61	*Kirby et al.* [1987]
dcc	−3.8	0	6.0	39	*Durham et al.* [1997]
gbs	−2.4	1.4	1.8	49	*Goldsby and Kohlstedt* [2001]
basal	7.74	0	2.4	60	*Goldsby and Kohlstedt* [2001]
diff	−3.46	2	1.0	59.4	*Goldsby and Kohlstedt* [2001] *Bland and Showman* [2007]

[a]Here *dca*, *dcb*, and *dcc* are for dislocation creep *a*, *b*, and *c*, respectively; *diff*, *basal*, and *gbs* are for diffusion flow, basal slip, and grain boundary sliding, respectively.

where $\dot{\varepsilon}_{diff}$, $\dot{\varepsilon}_{basal}$, and $\dot{\varepsilon}_{gbs}$ are the strain rate for diffusion flow, basal slip, and grain boundary sliding, respectively; and $\dot{\varepsilon}_{dca}$, $\dot{\varepsilon}_{dcb}$, and $\dot{\varepsilon}_{dcc}$ are the strain rate for dislocation creep *a*, *b*, and *c*, respectively. The rheological parameters used in this work are summarized in Table 3. The strain rate for a single mechanism $\dot{\varepsilon}_j$ is

$$\dot{\varepsilon}_j = \frac{A\sigma^n}{d^p} e^{-Q/RT} \tag{18}$$

where A is a constant, σ is the differential stress, d is the grain size, R is the gas constant, Q is the activation energy, T is temperature, and n and p are constants. The flow law for diffusion creep is given adopting equation (18) and defining an effective A [*Barr and Pappalardo*, 2005; *Bland and Showman*, 2007]. The ice grain size is not well constrained in Titan's ice I shell. We adopt a reference grain size of 0.1–1.0 mm consistent with current literature on icy satellites tectonism [*McKinnon*, 2006; *Bland and Showman*, 2007].

[28] Plastic deformation is modeled with the Drucker-Prager yield criterion [*Drucker and Prager*, 1952]. Plasticity gives a continuum representation of the brittle behavior of the ice during lithospheric deformation. The yielding criterion is given by

$$\alpha I_1 + \sqrt{I_2} = k \tag{19}$$

where α and k are material parameters written as

$$\alpha = \frac{2\sin\varphi}{\sqrt{3}(3-\sin\varphi)},\ k = \frac{2C\cos\varphi}{\sqrt{3}(3-\sin\varphi)} \tag{20}$$

and C is the cohesion, φ is the angle of internal friction; I_1 and I_2 are the first and second invariants of the stress tensor σ_{ij}

$$I_1 = \sigma_{kk} \tag{21}$$

$$I_2 = \frac{1}{2}\left(\sigma_{ij}\sigma_{ij} - \sigma_{ii}\sigma_{ii}\right) \tag{22}$$

[29] We consider a cohesion C of 10 MPa and an angle of internal friction φ of 30° [*Beeman et al.*, 1988; *Bland and Showman*, 2007].

[30] In the simulations we adopt a linear temperature gradient given by Fourier's law within the ice I shell and a surface temperature of 94 K. We use a temperature cutoff of 180 K at depth to avoid numerical instabilities of the code. We impose a small amplitude (~10 m) and polyharmonic topographic perturbation on the top surface of the domain.

3.2. Results From Tekton: Predicting Folds

[31] Results of our numerical simulations show that for low temperature gradients in the ice I shell (a few K km^{-1}), contractional lithospheric deformation should produce polyharmonic and asymmetric folds with topographic heights ~100 m (Figure 2). For higher temperature gradients and large strain (10 K km^{-1} and 0.158 in Figures 2 and 3), contractional lithospheric deformation produces harmonic and cylindrical folding with topographic heights on the order of several kilometers. For example, simulations with a strain of 0.158 and strain rate $5{\cdot}10^{-15}$ s^{-1} can produce a mountain chain wavelength of ~50 km and a topographic height of 2.7 km (Figure 3). Folds can develop from brittle faults, but the wavelengths of folds do not require the formation of thrusts [*Gerbault et al.*, 1999].

[32] We found that the imposed initial topographic perturbations can produce changes in fold formation. However, the resulting folds show similar final form if we adopt different polyharmonic initial perturbations. Figure 4 shows two examples obtained with two different initial perturbations. Figures 4a and 4c show the initial perturbations and the Figures 4b and 4d show the final deformation. Figures 4a and 4b show the simulation results in Figure 3 that were obtained by adopting an initial perturbation with 16 wavelengths and a small amplitude of ~10 m. Figures 4c and 4d show numerical simulation results with the same conditions of the previous simulation, but obtained adopting an initial polyharmonic perturbation with 32 wavelengths and a small amplitude of ~10 m.

[33] Temperature gradients of ~10 K km^{-1} correspond to an ancient high heat flux of the order of ~0.03–0.06 W m^{-2}, depending on the thermal conductivity of the ice shell. Such high heat flux (a factor of three to six times the calculated present-day flux [*Tobie et al.*, 2005; *Mitri and Showman*, 2008]) might have been produced during interior differentiation, by radiogenic decay and/or tidal friction. The heat flux of ~0.03 W m^{-2} corresponds to the heat flux at the onset of convection in the ice I shell (Figure 1); the global volume change model shows that the same heat flux corresponds to a large (~2 km) and relatively fast (~10^7 yr) radial contraction of Titan. After the onset of convection in the ice I shell, Titan might contract by ~7 km on time scales of the order of 10^8–10^9 yr (see section 2.2). While this link between the two models is interesting, it should be noted that the onset of convection is not a requirement for radial contraction to occur (Figure 1).

[34] A temperature gradient of ~10 K km^{-1} might correspond to a lower heat flux (~0.02 W m^{-2}) if a substantial amount of clathrate were present in the ice I shell, because

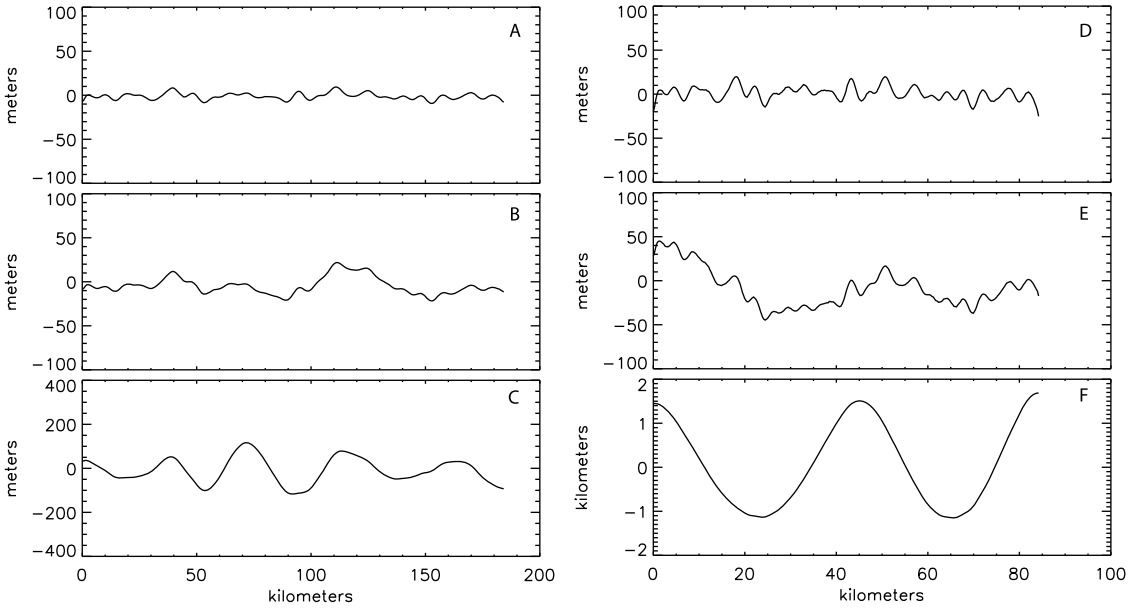

Figure 2. Topography produced by contractional lithospheric deformation of the ice I shell. Figures 2a–2c are for a strain of 0.079 and a strain rate of $2.5 \cdot 10^{-15}$ s^{-1}. The temperature gradients in the ice I shell are (a) 2 K km^{-1}, (b) 5 K km^{-1}, and (c) 10 K km^{-1}. The initial two-dimensional domain is 200 km by 25 km. Figures 2d–2f are for a strain of 0.158 and a strain rate is $5 \cdot 10^{-15}$ s^{-1}. The temperature gradients in the ice I shell are (d) 2 K km^{-1}, (e) 5 K km^{-1}, and (f) 10 K km^{-1}. The initial two-dimensional domain is 100 km by 25 km. All the simulations are for an ice grain size of 1 mm, Young's modulus of $9 \cdot 10^9$ Pa, and Poisson's ratio of 0.314. For all the simulations we adopt an initial polyharmonic perturbation with 16 wavelengths and amplitude ~10 m.

the presence of the clathrate would significantly reduce the thermal conductivity of the ice [*Tobie et al.*, 2006]. Figures 2 and 3 show that to produce folds with a topographic height of a few kilometers a high strain (0.158 for model presented in Figure 3) is necessary. Such local high strain is not inconsistent with global lower strain as predicted by the global radial contraction. As observed on Ganymede, strained craters suggest large local strains but this does not imply that the global strain is nearly as large.

[35] Folds produced during lithospheric contractional deformation would experience viscous relaxation as shown by Figure 5. A contractional strain of 0.158 was imposed over the first 1 Myr, and the folds are then allowed to relax over the next 99 Myr. The temperature gradient in the ice I shell is 10 K km^{-1}, the grain size is 1 mm, the Young's modulus is $9 \cdot 10^9$ Pa, and Poisson's ratio is 0.314. The initial two-dimension domain is 100 km by 25 km with a spatial resolution of 333 m for each element. The time step for contraction is 10 yr and for relaxation is 10^3 yr. (Numerical simulation of relaxation with a time step of 10 yr produces identical results to that with a time step of 10^3 yr.) To first order, the viscous relaxation does not depend on the lithospheric contraction. However, Figure 5 shows that the residual stress after contraction (1.0–1.1 Myr in the plot) would build up topography of ~100 m also in absence of strain. Figure 5 demonstrates that little relaxation occurs, suggesting that fold topography can be maintained over long time periods at the thermal gradients explored here.

[36] In summary, we have demonstrated using finite element Tekton code that Titan's global volume change can produce folding. A temperature gradient ~10 K km^{-1} necessary to produce such folds corresponds to an ancient high heat flux of approximately 0.03–0.06 W m^{-2}. This thermal gradient corresponds to a temperature gradient at the onset of convection in the ice I shell and subsequent relatively rapid global radial contraction of Titan; however, it is important to note that the onset of convection is not a requirement for radial contraction to occur (Figure 1). The thermal gradient found could correspond to a lower heat flux (~0.02 W m^{-2}) that could be explained by the presence of clathrates. Finally, we have demonstrated that little viscous relaxation occurs, indicating that Titan's contractional tectonic structures should endure for long time periods.

4. Titan's Mountains: Evidence of Folding?

[37] If radial contraction is predicted to produce folds, then it is natural to consider whether Titan displays folds, formed as an expression of contractional deformation of the ice lithosphere. Topographic information is important to that assessment and can be derived from SARTopo and radarclinometry techniques, described next.

4.1. SARTopo

[38] The derivation of SARTopo [*Stiles et al.*, 2009] is based upon Amplitude Monopulse Comparison [*Chen and Hensley*, 2005], which permits extraction of topographic data that is cospatial with the image data. The data is model-independent, and is not reliant on overlap between SAR scenes. The SARTopo method estimates surface heights by comparing the calibration of overlapping Titan SAR imagery

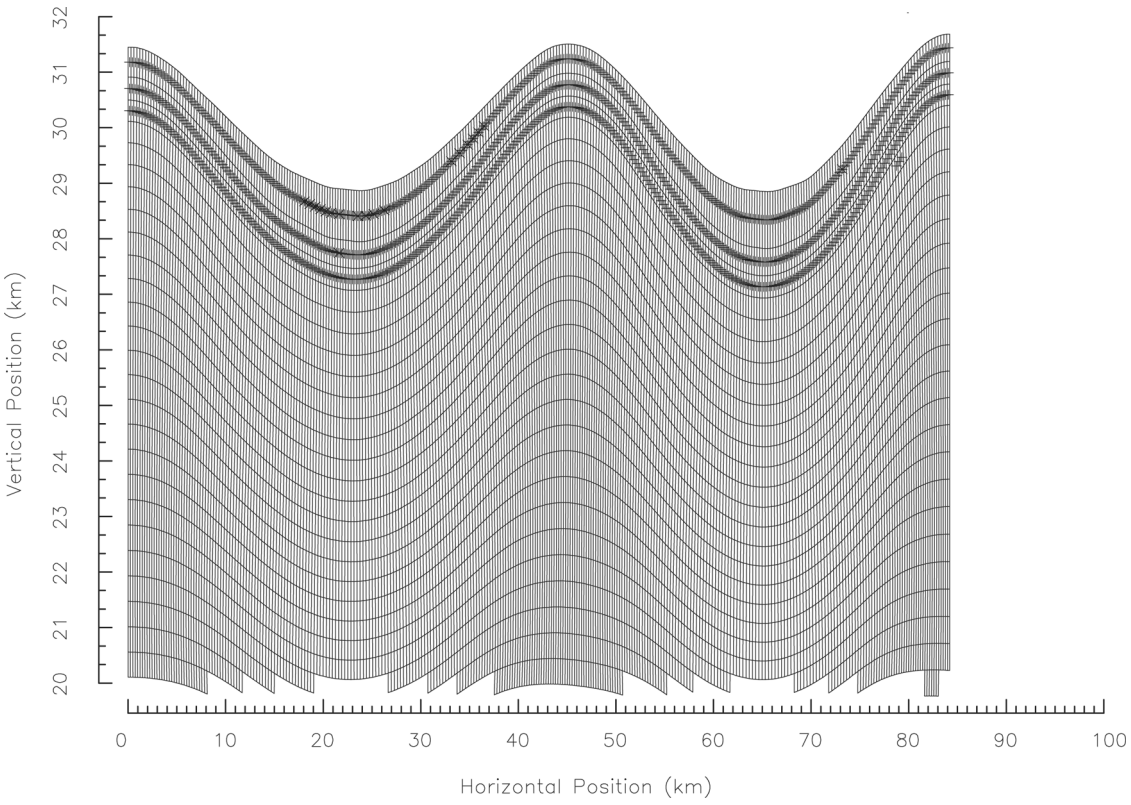

Figure 3. Topography produced by contractional deformation of the icy lithosphere. The strain is 0.158, the strain rate is $5 \cdot 10^{-15}$ s^{-1}, and the temperature gradient in the ice I shell is 10 K km^{-1}. The simulations are for an ice grain size of 1 mm, Young's modulus of $9 \cdot 10^9$ Pa, and Poisson's ratio of 0.314. The constitutive rheologies of the viscous flow are based on laboratory measurements [*Kirby et al.*, 1987; *Durham et al.*, 1997; *Goldsby and Kohlstedt*, 2001]. Plastic deformation is modeled with a Drucker-Prager yield criterion with a cohesion coefficient 10 MPa and an angle of internal friction 30°. The initial two-dimensional domain is 100 km by 25 km with a spatial resolution of 333 m for each element. The time step is 10 yr. Identical results are produced by numerical simulations with an initial two-dimensional domain of 100 km by 50 km with a spatial resolution of 333 m for each element and with an initial two-dimensional domain of 200 km by 50 km with a spatial resolution of 500 m for each element.

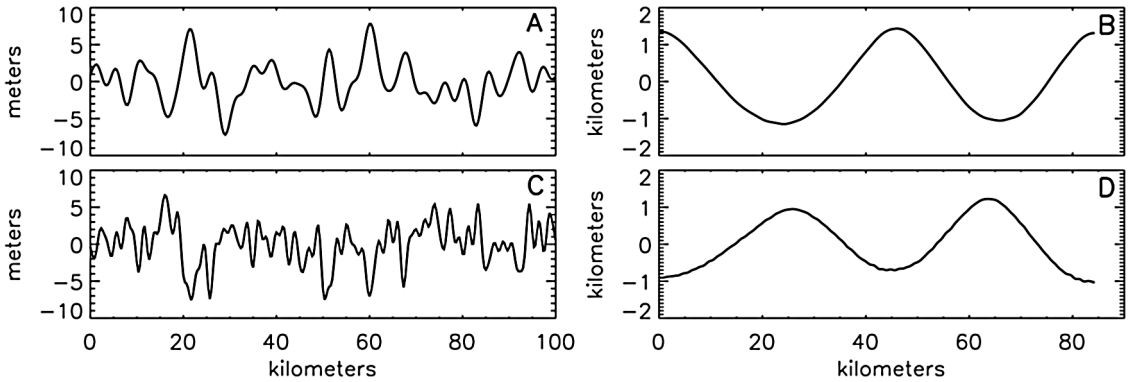

Figure 4. Influence of initial topographic perturbations on fold formation. Figures 4a and 4c show the initial perturbations, and Figures 4b and 4d show the final deformation. (a and b) The simulation results obtained by adopting an initial perturbation with 16 wavelengths and a small amplitude of ~10 m. (c and d) Numerical simulation results with the same conditions as the previous simulation but obtained adopting an initial polyharmonic perturbation with 32 wavelengths and a small amplitude of ~10 m. The strain is 0.158, the strain rate is $5 \cdot 10^{-15}$ s^{-1}, and the temperature gradient in the ice I shell is 10 K km^{-1}. The simulations are for an ice grain size of 1 mm, Young's modulus of $9 \cdot 10^9$ Pa, and Poisson's ratio of 0.314.

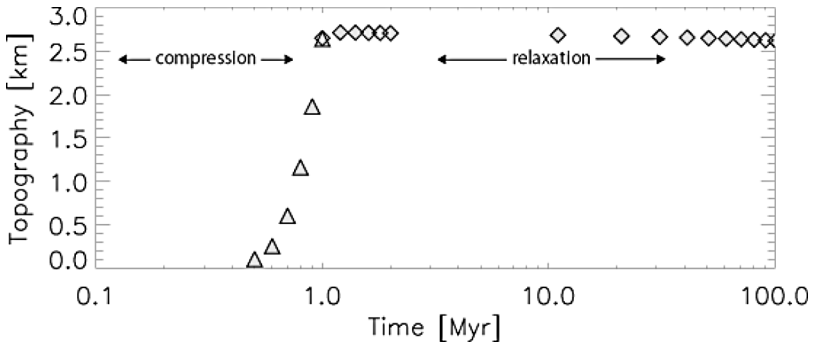

Figure 5. Fold formation and relaxation. A contractional strain of 0.158 was imposed over the first 1 Myr. The folds are then allowed to relax over the next 99 Myr. The temperature gradient in the ice I shell is 10 K km^{-1}, the grain size is 1 mm, Young's modulus is $9{\cdot}10^9$ Pa, and Poisson's ratio is 0.314. The initial two-dimension domain is 100 km by 25 km with a spatial resolution of 333 m for each element. The time step for contraction is 10 yr and for relaxation is 10^3 yr. Numerical simulation of relaxation with a time step of 10 yr (between 1 and 2 Myr in the plot) produces identical results to that with a time step of 10^3 yr.

within a single SAR observation obtained from different antenna feeds of the Cassini Radar instrument. Cassini Radar employs five different antenna feeds that are cycled in order to obtain a wide swath on the ground. The antenna footprints produced by the feeds overlap substantially. Because the overlapping scenes are observed from nearly identical incidence angles, they are unsuitable for stereo processing. However, given sufficiently accurate knowledge of spacecraft pointing and ephemeris and the antenna beam patterns, the height of the surface can be estimated from the apparent backscatter calibration differences in the overlapping scenes. We also vary the local Titan radius used to process the images and select the surface height that minimizes the calibration mismatch between the two feeds. The SARTopo technique has been validated by comparison with overlapping nadir-pointing radar altimetry, and the comparison yields an absolute bias of 150 m and relative errors less than 50 m. The SARTopo technique is fully described by *Stiles et al.* [2009].

4.2. Radarclinometry

[39] Radarclinometry can also be used to constrain topographic heights on Titan. Radarclinometry, similar to the technique of photoclinometry, utilizes brightness variations as detected by the SAR instrument to construct slopes, based on an assumed model backscatter law. Endpoints of peak traces are anchored at equal elevations, and then slopes are integrated one-dimensionally to infer topographic heights [*Kirk et al.*, 2005; *Radebaugh et al.*, 2007]. Cross-profile slopes are assumed to be zero for these calculations. Mountainous regions over which we have applied the radarclinometry technique are assumed to be of uniform radar brightness. Thus, radarclinometry passes are kept short, typically under 20 km. Although materials are not expected to be completely uniform across distances of 20 km, this assumption is likely adequate.

4.3. Morphological Evidence From Cassini Radar Data

[40] Cassini remote sensing observations of Titan provide evidence for "mountains," relatively rough (radar bright) features, which are elevated above the surrounding landscape [*Radebaugh et al.*, 2007]. The mean mountain height above the surrounding landscape is derived using radarclinometry, as imaged by the Cassini Radar instrument during the T3 flyby (February 2005) and the T8 flyby (October 2005), is ~860 m and the topographic heights range up to 2 km [*Radebaugh et al.*, 2007]. Both isolated mountain blocks and linear mountain chains (200–300 km long) are observed [*Radebaugh et al.*, 2007]. The Huygens Descent Imager Spectral Radiometer (DISR) has also shown that the topography close to the Huygens landing site is ~100–150 m higher than that of the surrounding plains [*Tomasko et al.*, 2005]. During the T20 flyby (October 2006), the Visual and Infrared Mapping Spectrometer (VIMS) instrument observed putative large mountains chains (150 km and 30 km wide) south of Titan's equator [*Barnes et al.*, 2007].

4.4. Analysis of Possible Folds on Titan

[41] We use Synthetic Aperture Radar (SAR) imagery, and radarclinometric and SARTopo techniques to study morphological aspects of probable tectonic features on Titan. Region 1 presents a mountain block near 52°N, 13°E (Figure 6) [see also *Stiles et al.*, 2009, Figure 12]. Figure 6 also shows a SARTopo profile crossing this mountain block, demonstrating that its height above the surroundings is ~1,400 m. The region near −30°S, −107°W (hereafter called region 2; Figure 7), the region on the NW border of Xanadu near −2°S, −127°W (hereafter called region 3; Figure 8), imaged by the Cassini Radar during the T43 flyby (May 2008), the region near −10°S, 145°E (hereafter called region 4; Figure 9) [see also *Radebaugh et al.*, 2007, Figure 5] imaged during the T8 flyby (October 2005) all show parallel mountains chains in adjacent regions. Using the SARTopo technique, we find that the maximum topographic height of the mountains relative to the surrounding plains in region 2 is ~800 m (Figure 7). Using the radarclinometric technique, we find that the maximum topographic height of the mountains relative to the surrounding plains in region 3 is ~2,000 m (Figure 8). Finally, using both the SARTopo and radarclinomeric techniques, we find that the maximum topographic height of the mountains relative to the surrounding plains in region 4 is 300–500 m (Figure 9). SARTopo data reveal that the mountain chains in regions 2, 3 and 4 are in areas that are elevated with respect to the surrounding terrains. Hereafter we refer to these elevated regions as highland terrains,

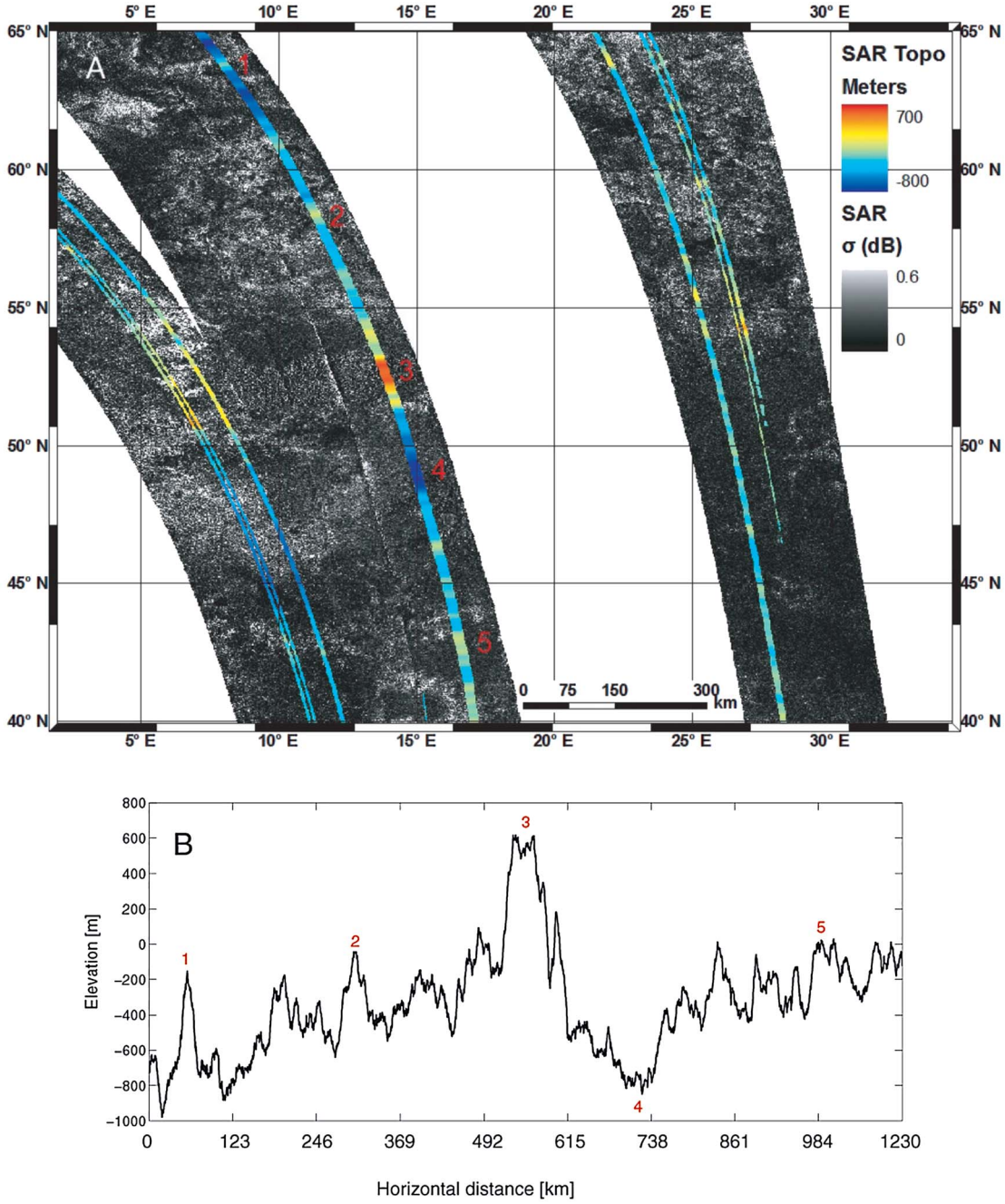

Figure 6. Region 1 (52°N, 13°E). (a) SARTopo traces (colored lines) are shown on Cassini Radar SAR swaths. (b) SARTopo profile from 65°N, 7°E to 40°N, 17°E crossing a mountain block imaged in Figure 6a. The red numbers correspond to the same features in Figures 6a and 6b.

in contrast to radar dark plains in this area which are interpreted to be regions in which organic materials have accumulated as sediments.

[42] The moderate resolution of the Cassini SAR imagery does not permit an unambiguous geological interpretation of the features presented here. Terrestrial analogs may provide insight into the geological setting of these mountainous regions on Titan. Valleys and linear, subparallel features observed in regions 1, 2, 3 and 4 show some morphological similarities with half grabens and rift systems such as the Basin and Range Province in the western United States, which were formed by stretching of the lithosphere. However, the mountainous regions on Titan investigated here also present some morphological similarities to the valleys and fold-thrust belts of the Zagros Mountains in Iran, which were formed by shortening of the terrestrial lithosphere.

[43] Let us consider the case of simple stretching of the lithosphere. In general, stretching produces thinning of the lithosphere and subsidence, and could involve the formation of grabens and horsts, as well as half grabens. The presence

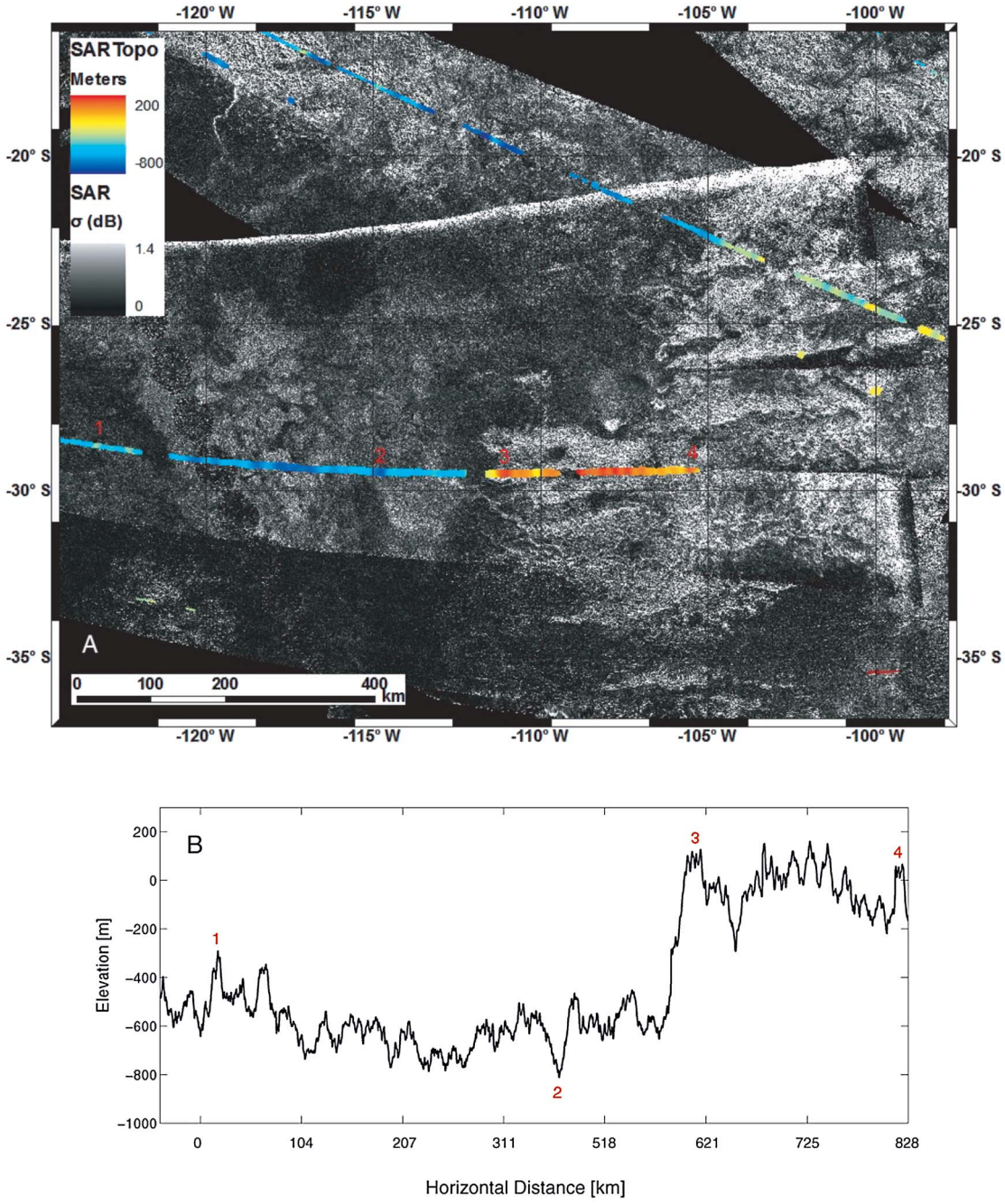

Figure 7. Region 2 (−30°S, −107°W). (a) SARTopo traces (colored lines) are shown on Cassini Radar SAR swaths. (b) SARTopo profile from −125°W to −105°W. The red numbers correspond to the same features in Figures 7a and 7b.

of mountains (in particular on regions 2, 3 and 4) on highland terrains is not consistent with subsidence. We could also invoke a more complex geological scenario, such as stretching of the lithosphere over a zone of upwelling, similar to the tectonic processes that have produced the Grand Teton Mountains in the central United States. While such scenarios cannot be eliminated, large extensional strains of the lithosphere in other icy satellites such as Ganymede and Europa have produced radically different structures compared to the mountainous regions 1, 2, 3 and 4 on Titan, such as grooved terrains on Ganymede and bands on Europa.

[44] Contractional features on icy satellites are not without precedent, as folds with a height of the order of hundreds of meters are present on Europa [*Prockter and Pappalardo*, 2000]. Shortening of the lithosphere and the formation of folds and fold-thrust belts produces thickening and uplift, which would be consistent with mountainous regions 2, 3

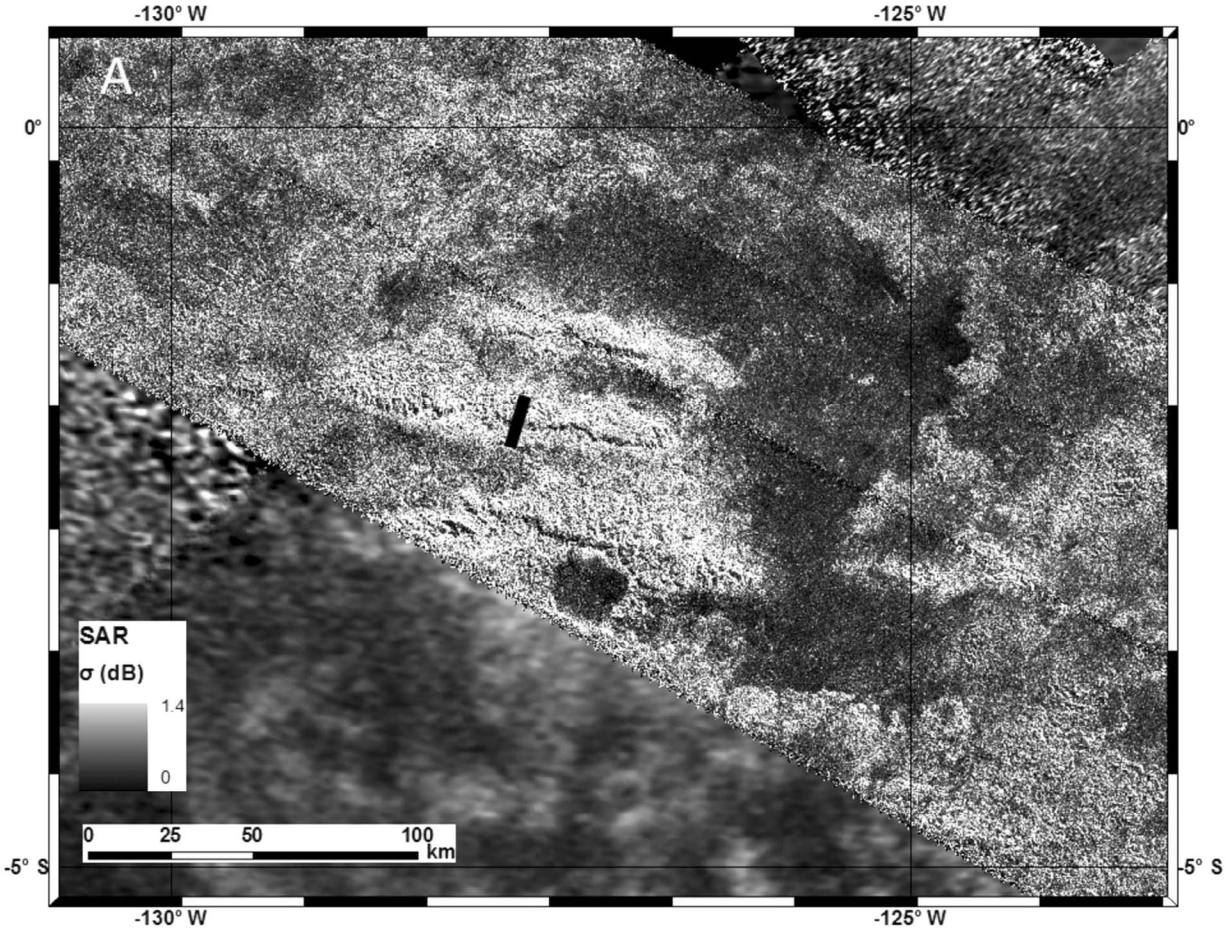

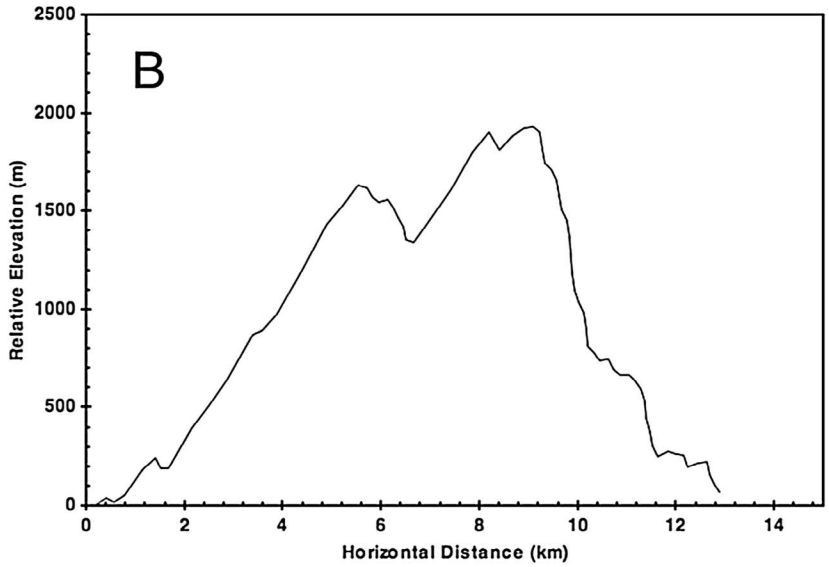

Figure 8. Region 3. (a) Cassini Radar SAR imagery show elongate three radar bright features. (b) Radarclinometric profile (black line in Figure 8a) for a representative portion of the T43 swath containing the Region 3 ridges reveals heights up to 1,930 m. Measurements in other regions on this ridge and on the other ridges yielded similar results. A cosine (incidence angle) model, similar to that of *Radebaugh et al.* [2007], was used to calculate slopes, corresponding to model brightnesses and related heights. 90th percentile slopes measure 30 degrees. Radar shadowing likely occurs in several pixels with low brightnesses, but their small numbers mean that slope calculations are not severely affected.

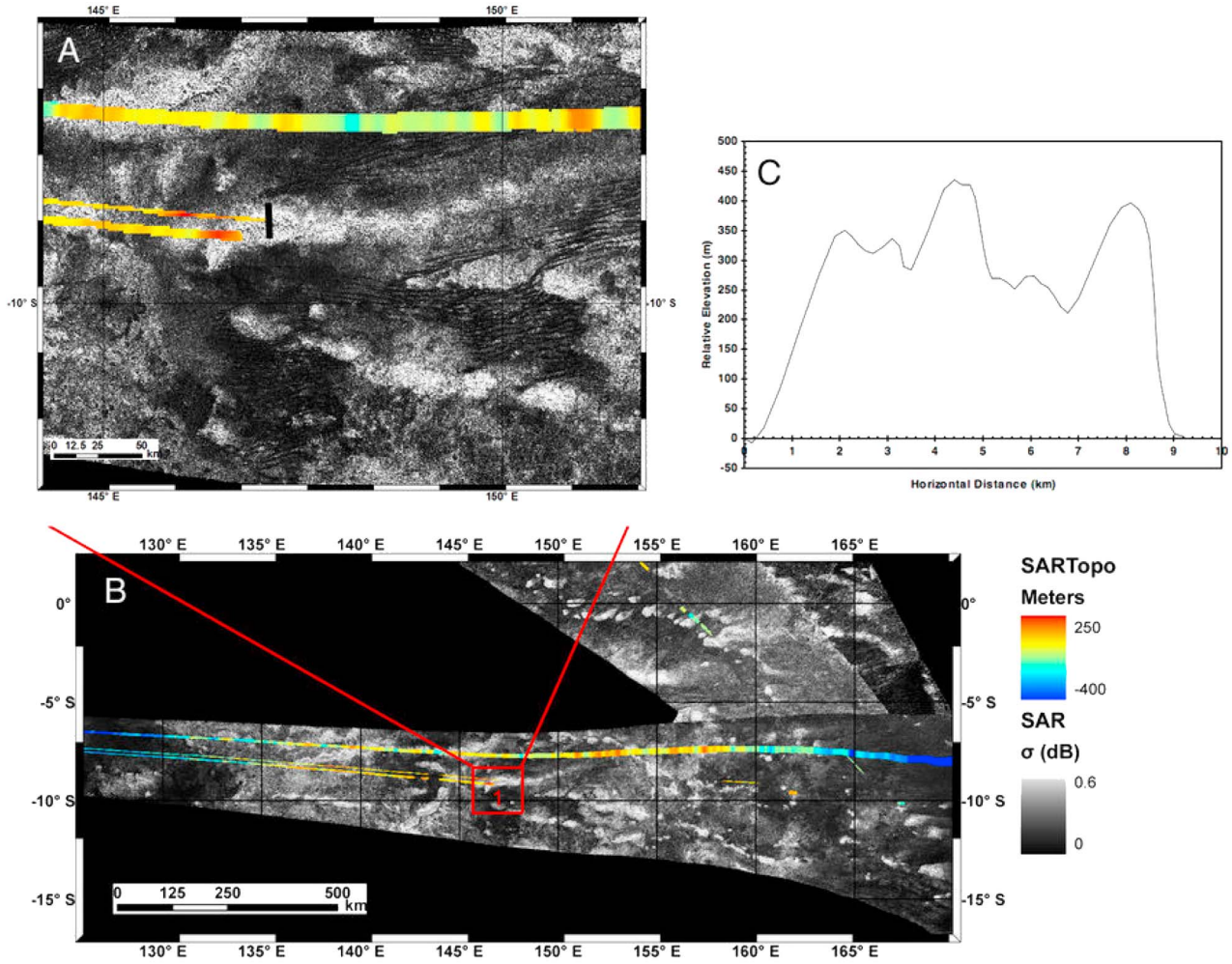

Figure 9. Region 4 (−10°S, 147°E). (a) Cassini Radar SAR imagery shows radar bright features. (b) SARTopo traces (colored lines) are shown on Cassini Radar SAR swaths. (c) Radarclinometric profile (black line in Figure 9a) for a representative portion of the swath containing the Region 4 ridges reveals heights up to 450 m.

and 4 being located on highland terrains. If contractional tectonism has played a role on Titan, this bespeaks of a relatively complex history that cannot be explained with a single geological process or event.

5. Discussion

[45] The interior of Titan is inferred to be at least partially differentiated into a rocky or a mixture of rock and ice deep interior, a high-pressure ice layer (with phases III, V, and VI), a subsurface liquid layer (ocean), and an outer ice I shell [*Mitri et al.*, 2010]. Tidal evolution and the radiogenic decay in the interior caused a gradual cooling of Titan [*Tobie et al.*, 2005, 2006]. The long-term cooling caused thickening of the ice I, III, V and VI layers, and freezing of the subsurface ocean over a time scale on the order of 10^8–10^9 yr. Because of the density differences among the ice I layer, the high-pressure ice layer, and the liquid layer, we have found that the freezing of the subsurface ocean causes a global radial contraction of Titan.

[46] We have assumed that ammonia is the main component of the subsurface water ocean. The presence of ammonia decreases the mean density of the liquid layer facilitating the global radial contraction of Titan during its cooling. However, we have also found that for small concentrations of ammonia in the liquid layer and at the limit of a pure water ocean, radial contraction occurs during the evolution of Titan.

[47] The liquid layer of Titan is also expected to contain salts, which increase the density of the liquid layer, inducing the opposite effect of ammonia in terms of volume change. The detection of an induced magnetic field indicates that the liquid layer of Europa contains salts [*Zimmer et al.*, 2000]. Considering a conductivity of ~116 mS m^{-1} and a depth of 100 km for the liquid layer [*Zimmer et al.*, 2000], *Melosh et al.* [2004] roughly estimated a salinity of ~0.1% for Europa's ocean. We can also use this value as a reference value for the salinity of Titan's liquid layer. Terrestrial seawater has a higher salinity of ~3–4% and a reference density

of 1,020–1,030 kg m^{-3}. Therefore, given the plausible concentration of salts present in the subsurface liquid layer, ammonia could be the major contributor in terms of the ocean's density for global volume changes as compared to the salinity.

[48] A global radial contraction during the gradual cooling of Titan would produce lithospheric shortening. We have studied the predicted tectonic implications of such contraction. Our Tekton folding model predicts long-wavelength, cylindrically shaped folds may occur on Titan, resulting from lithospheric shortening. Folds could potentially achieve a topographic height of several kilometers for high temperature gradients in the ice I shell (~10 K km^{-1}), corresponding to an ancient high heat flux from the interior (~0.02–0.06 W m^{-2}). A tectonic episode can also be produced in thermal models in which the ice I shell transitioned from a conductive state to a convective state [*Mitri and Showman*, 2008]. Perhaps the orogenesis of many of Titan's mountains occurred during such an era of transition, when Titan's interior was warmer than present-day, but then the lithosphere became increasingly thick and rigid, allowing the more effective preservation of surface features.

[49] Examination of Synthetic Aperture Radar (SAR) imagery obtained by Cassini Radar along with derived topographic information shows possible evidence of contractional tectonism in the equatorial regions of Titan, although the moderate resolution of the Cassini SAR imagery does not permit an unambiguous geological interpretation. Several mountain chains on Titan are localized in equatorial latitudes and have a general west-east orientation. Coupled with the lack of similar equatorial chains oriented in other directions, this suggests a possible common origin of these mountain chains, plausibly as contractional. Radial contraction could produce regionally large lithospheric strain compared to the overall global value. However, global contraction should produce an isotropic stress field on Titan's surface that does not favor any specific orientation of tectonic features. Perhaps during the satellite's contraction additional nonisotropic stresses not modeled here would yield preferential orientations of tectonic structures on a global scale.

[50] It is remarkable that different thermal-orbital evolutions and internal structures have conspired to produce significant differences in the respective tectonic styles of icy satellites. Ganymede's surface is characterized by extensional tectonism manifested as grooved terrains. Passage through an eccentricity-pumping resonance during Ganymede's evolution could have led to global thermal runaway of Ganymede [*Showman et al.*, 1997; *Bland et al.*, 2009]. During the largest thermal runaway, Ganymede could have undergone significant melting of the ice I shell and high-pressure layer and, consequently, global volume expansion and formation of grooved terrains [*Showman et al.*, 1997; *Bland et al.*, 2009]. *McKinnon* [2006] has argued that Callisto probably had a convecting ice I shell in the past, and a transition from convection to conduction would cause a great thinning of the ice shell, volume change, and consequent tectonics. Because these effects are not observed, McKinnon concluded that the ice I shell must still be convecting today.

[51] Extensional tectonism is observed on almost all icy satellites of the outer solar system, but we have little evidence of contractional tectonism on icy satellites. If in fact most of Titan's mountains were due to contractional tectonism, then Titan would be the only icy satellite on which contraction is the predominant style of tectonism.

[52] **Acknowledgments.** Much of this work was carried out at the Jet Propulsion Laboratory, California Institute of Technology under a contract from NASA. We thank the Cassini Radar team. G.M. is grateful to Alex Hayes. J.I.L. and G.M. thank Angioletta Coradini for her hospitality at the Institute for the Physics of Interplanetary Space in Roma (Italy), where some of the research was conducted. A.P.S. was supported by NASA PG&G grant NNX07AR27G.

References

Anderson, J. D., G. Schubert, R. A. Jacobson, E. L. Lau, W. B. Moore, and W. L. Sjogren (1998), Europa's differential internal structure: Inferences from four Galileo encounters, *Science*, *281*, 2019–2022, doi:10.1126/science.281.5385.2019.

Barnes, J. W., et al. (2007), Near-infrared spectral mapping of Titan's mountains and channels, *J. Geophys. Res.*, *112*, E11006, doi:10.1029/2007JE002932.

Barr, A. C., and R. T. Pappalardo (2005), Onset of convection in the icy Galilean satellites: Influence of rheology, *J. Geophys. Res.*, *110*, E12005, doi:10.1029/2004JE002371.

Beeman, M., W. B. Durham, and S. H. Kirby (1988), Friction of ice, *J. Geophys. Res.*, *93*, 7625–7633, doi:10.1029/JB093iB07p07625.

Bland, M. T., and A. P. Showman (2007), The formation of Ganymede's grooved terrain: Numerical modeling of extensional necking instabilities, *Icarus*, *189*, 439–456, doi:10.1016/j.icarus.2007.01.012.

Bland, M. T., A. P. Showman, and G. Tobie (2009), The orbital-thermal evolution and global expansion of Ganymede, *Icarus*, *200*, 207–221, doi:10.1016/j.icarus.2008.11.016.

Chen, C. W., and S. Hensley (2005), Amplitude-based height-reconstruction techniques for synthetic aperture ladar systems, *J. Opt. Soc. Am. A*, *22*(3), 529–538, doi:10.1364/JOSAA.22.000529.

Choukroun, M., and O. Grasset (2007), Thermodynamic model for the water and high-pressure ices up to 2.2 GPa and down to the metastable domain, *J. Chem. Phys.*, *127*, 124506, doi:10.1063/1.2768957.

Collins, G. C., W. B. McKinnon, J. M. Moore, F. Nimmo, R. T. Pappalardo, L. M. Prockter, and P. M. Schenk (2009), Tectonics of the outer planet satellites, in *Planetary Tectonics*, edited by R. A. Schultz and T. R. Watters, pp. 264–350, Cambridge Univ. Press, New York, doi:10.1017/CBO9780511691645.008.

Croft, S. K., J. I. Lunine, and J. Kargel (1988), Equation of state of ammonia-water liquid, *Icarus*, *73*, 279–293, doi:10.1016/0019-1035(88)90098-X.

Drucker, D. C., and W. Prager (1952), Soil mechanics and plastic analysis for limit design, *Q. Appl. Math.*, *10*(2), 157–165.

Dumoulin, C., M. P. Doin, and L. Fleitout (1999), Heat transport in stagnant lid convection with temperature- and pressure-dependent Newtonian or non-Newtonian rheology, *J. Geophys. Res.*, *104*, 12,759–12,777, doi:10.1029/1999JB900110.

Durham, W. B., S. H. Kirby, and L. A. Stern (1997), Creep of water ices at planetary conditions: A compilation, *J. Geophys. Res.*, *102*, 16,293–16,302, doi:10.1029/97JE00916.

Fortes, A. D., P. M. Grindrod, S. K. Trickett, and L. Vocadlo (2007), Ammonium sulfate on Titan: Possible origin and role in cryovolcanism, *Icarus*, *188*, 139–153, doi:10.1016/j.icarus.2006.11.002.

Gammon, P. H., H. Klefte, and M. J. Clouter (1983), Elastic constants of ice samples by Brillouin spectroscopy, *J. Phys. Chem.*, *87*, 4025–4029, doi:10.1021/j100244a004.

Gerbault, M., E. B. Burov, A. N. B. Poliakov, and M. Daignières (1999), Do faults trigger folding in the lithosphere?, *Geophys. Res. Lett.*, *26*, 271–274, doi:10.1029/1998GL900293.

Goldsby, D. L., and D. L. Kohlstedt (2001), Superplastic deformation of ice: Experimental observations, *J. Geophys. Res.*, *106*, 11,017–11,030, doi:10.1029/2000JB900336.

Grasset, O., C. Sotin, and F. Deschamps (2000), On the internal structure and dynamics of Titan, *Planet. Space Sci.*, *48*, 617–636, doi:10.1016/S0032-0633(00)00039-8.

Hutter, K. (1983), *Theoretical Glaciology: Material Science of Ice and the Mechanics of Glaciers and Ice Sheets*, D. Reidel, Tokyo.

Iess, L., N. J. Rappaport, R. A. Jacobson, P. Racioppa, D. J. Stevenson, P. Tortora, J. W. Armstrong, and S. W. Asmar (2010), Gravity field, shape, and moment of inertia of Titan, *Science*, *327*, 1367–1369, doi:10.1126/science.1182583.

Kirby, S. H., W. B. Durham, M. L. Beeman, H. C. Heard, and M. A. Daley (1987), Inelastic properties of ice Ih at low temperatures and high pressures, *J. Phys.*, *48*, 227–232.

Kirk, R. L., P. Callahan, R. Seu, R. D. Lorenz, F. Paganelli, R. M. Lopes, C. Elachi, and the Cassini Radar Team (2005), Radar reveals Titan topography, *Lunar Planet. Sci.*, *XXXVI*, Abstract 2227.

Lorenz, R. D., B. W. Stiles, R. L. Kirk, M. D. Allison, P. Persi del Marmo, L. Iess, J. I. Lunine, S. J. Ostro, and S. Hensley (2008), Titan's rotation reveals an internal ocean and changing zonal winds, *Science*, *319*, 1649–1651, doi:10.1126/science.1151639.

Lunine, J. I., and D. J. Stevenson (1987), Clathrate and ammonia hydrates at high pressure: Application to the origin of methane on Titan, *Icarus*, *70*, 61–77, doi:10.1016/0019-1035(87)90075-3.

Mamayev, O. I. (1975), *Temperature-Salinity Analysis of World Ocean Waters*, Elsevier Sci., Amsterdam.

Manga, M., and C. Y. Wang (2007), Pressurized oceans and the eruption of liquid water on Europa and Enceladus, *Geophys. Res. Lett.*, *34*, L07202, doi:10.1029/2007GL029297.

McKinnon, W. B. (1999), Convective instability in Europa's floating ice shell, *Geophys. Res. Lett.*, *26*, 951–954, doi:10.1029/1999GL900125.

McKinnon, W. B. (2006), On convection in ice I shells of outer Solar System bodies, with detailed application to Callisto, *Icarus*, *183*, 435–450, doi:10.1016/j.icarus.2006.03.004.

Melosh, H. J., and A. Raefsky (1980), The dynamical origin of subduction zone topography, *Geophys. J. R. Astron. Soc.*, *60*, 333–354.

Melosh, H. J., A. G. Ekholm, A. P. Showman, and R. D. Lorenz (2004), The temperature of Europa's subsurface water ocean, *Icarus*, *168*, 498–502, doi:10.1016/j.icarus.2003.11.026.

Mitri, G., and A. P. Showman (2005), Convective conductive transitions and sensitivity of a convecting ice shell to perturbations in heat flux and tidal-heating rate: Implications for Europa, *Icarus*, *177*, 447–460, doi:10.1016/j.icarus.2005.03.019.

Mitri, G., and A. P. Showman (2008), Thermal convection in ice-I shells of Titan and Enceladus, *Icarus*, *193*, 387–396, doi:10.1016/j.icarus.2007.07.016.

Mitri, G., R. T. Pappalardo, and D. J. Stevenson (2010), Evolution and interior structure of Titan, *Lunar Planet. Sci.*, *XLI*, Abstract 2229.

Mousis, O., D. Gautier, and A. Coustenis (2002), The D/H ratio in methane in Titan: Origin and history, *Icarus*, *159*, 156–165, doi:10.1006/icar.2002.6930.

Niemann, H. B., et al. (2005), The abundances of constituents of Titan's atmosphere from the GCMS instrument on the Huygens probe, *Nature*, *438*, 779–784, doi:10.1038/nature04122.

Nimmo, F. (2004), Stresses generated in cooling viscoelastic ice shells: Application to Europa, *J. Geophys. Res.*, *109*, E12001, doi:10.1029/2004JE002347.

Nimmo, F., and B. G. Bills (2010), Shell thickness variations and the long wavelength topography of Titan, *Icarus*, *208*, 896–904, doi:10.1016/j.icarus.2010.02.020.

Paganelli, F., et al. (2007), Titan's surface from Cassini Radar SAR and high resolution radiometry data of the first five flybys, *Icarus*, *191*, 211–222, doi:10.1016/j.icarus.2007.04.032.

Prockter, L. M., and R. T. Pappalardo (2000), Folds on Europa: Implications for crustal cycling and accommodation of extension, *Science*, *289*, 941–943, doi:10.1126/science.289.5481.941.

Radebaugh, J., R. D. Lorenz, R. L. Kirk, J. I. Lunine, E. R. Stofan, R. M. C. Lopes, S. D. Wall, and the Cassini Radar Team (2007), Mountains on Titan observed by Cassini Radar, *Icarus*, *192*, 77–91, doi:10.1016/j.icarus.2007.06.020.

Showman, A. P., D. J. Stevenson, and R. Malhotra (1997), Coupled orbital and thermal evolution of ganymede, *Icarus*, *129*, 367–383, doi:10.1006/icar.1997.5778.

Sohl, F., H. Hussmann, B. Schwentker, T. Spohn, and R. D. Lorenz (2003), Interior structure models and tidal Love numbers of Titan, *J. Geophys. Res.*, *108*(E12), 5130, doi:10.1029/2003JE002044.

Solomatov, V. S. (1995), Scaling of temperature- and stress-dependent viscosity convection, *Phys. Fluids*, *7*, 266–274, doi:10.1063/1.868624.

Solomatov, V. S., and L. N. Moresi (1996), Stagnant lid convection on Venus, *J. Geophys. Res.*, *101*, 4737–4753, doi:10.1029/95JE03361. (Correction, *J. Geophys. Res.*, *102*, 28,729, doi:10.1029/97JE02281, 1997.)

Solomatov, V. S., and L. N. Moresi (2000), Scaling of time-dependent stagnant lid convection: Application to small-scale convection on Earth and other terrestrial planets, *J. Geophys. Res.*, *105*, 21,795–21,817, doi:10.1029/2000JB900197.

Sotin, C., O. Grasset, and S. Beauchesne (1998), Thermodynamical properties of high-pressure ices: Implications for the dynamics and internal structure of large icy satellites, in *Solar System Ices*, *Astrophys. Space Sci. Lib. Ser.*, vol. 227, pp. 79–96, Kluwer Acad., Dordrecht, Netherlands.

Stiles, B.W., et al. (2008), Determining Titan's spin state from Cassini radar images, *Astron. J.*, *135*, 1669–1680.

Stiles, B. W., et al. (2009), Determining Titan surface topography from Cassini SAR data, *Icarus*, *202*, 584–598, doi:10.1016/j.icarus.2009.03.032.

Tobie, G., O. Grasset, J. I. Lunine, A. Mocquet, and C. Sotin (2005), Titan's internal structure inferred from a coupled thermal-orbital model, *Icarus*, *175*, 496–502, doi:10.1016/j.icarus.2004.12.007.

Tobie, G., J. I. Lunine, and C. Sotin (2006), Episodic outgassing as the origin of atmospheric methane on Titan, *Nature*, *440*, 61–64, doi:10.1038/nature04497.

Tomasko, M. G., et al. (2005), Rain, winds and haze during the Huygens probe's descent to Titan's surface, *Nature*, *438*, 765–778, doi:10.1038/nature04126.

Waite, H., et al. (2005), Ion-neutral mass spectrometer results from the first flyby of Titan, *Science*, *308*, 982–986, doi:10.1126/science.1110652.

Waite, J. H., Jr., et al. (2009), Liquid water on Enceladus from observations of ammonia and ^{40}Ar in the plume, *Nature*, *460*, 487–490, doi:10.1038/nature08153.

Zimmer, C., K. K. Khurana, and M. G. Kivelson (2000), Subsurface oceans on Europa and Callisto: Constraints from Galileo magnetometer observations, *Icarus*, *147*, 329–347, doi:10.1006/icar.2000.6456.

M. T. Bland, Department of Earth and Planetary Sciences, Washington University in Saint Louis, Saint Louis, MO 63130, USA.

R. M. C. Lopes, R. T. Pappalardo, and B. Stiles, Jet Propulsion Laboratory, California Institute of Technology, Pasadena, CA 91125, USA.

J. I. Lunine, Department of Physics, University of Rome Tor Vergata, via Orazio Raimondo 18, Rome I-00173, Italy.

G. Mitri, Division of Geological and Planetary Sciences, California Institute of Technology, MC 150-21, 1200 E. California Blvd., Pasadena, CA 91125, USA. (mitri@gps.caltech.edu)

J. Radebaugh, Department of Geological Sciences, Brigham Young University, Provo, UT 84602, USA.

A. P. Showman, Department of Planetary Sciences and Lunar and Planetary Laboratory, University of Arizona, Tucson, AZ 85721, USA.